



Evidence for Primordial Alignment: Insights from Stellar Obliquity Measurements for Compact Sub-Saturn Systems

Brandon T. Radzom¹ , Jiayin Dong^{2,8} , Malena Rice³ , Xian-Yu Wang¹ , Samuel W. Yee^{4,5,9} , Tyler R. Fairmington⁶ , Cristobal Petrovich^{1,7} , and Songhu Wang¹

¹ Department of Astronomy, Indiana University, 727 East 3rd Street, Bloomington, IN 47405-7105, USA

² Center for Computational Astrophysics, Flatiron Institute, 162 Fifth Avenue, New York, NY 10010, USA

³ Department of Astronomy, Yale University, 52 Hillhouse Ave, New Haven, CT 06511, USA

⁴ Center for Astrophysics | Harvard & Smithsonian, 60 Garden Street, Cambridge, MA 02138, USA

⁵ Department of Astrophysical Sciences, Princeton University, 4 Ivy Lane, Princeton, NJ 08544, USA

⁶ Centre for Astrophysics, University of Southern Queensland, West St, Darling Heights, Toowoomba, Queensland 4350, Australia

⁷ Millennium Institute for Astrophysics, Santiago, Chile

Received 2024 March 18; revised 2024 June 20; accepted 2024 July 8; published 2024 August 13

Abstract

Despite decades of effort, the mechanisms by which the spin axis of a star and the orbital axes of its planets become misaligned remain elusive. In particular, it is of great interest whether the large spin–orbit misalignments observed are driven primarily by high-eccentricity migration—expected to have occurred for short-period, isolated planets—or reflect a more universal process that operates across systems with a variety of present-day architectures. Compact multiplanet systems offer a unique opportunity to differentiate between these competing hypotheses, as their tightly packed configurations preclude violent dynamical histories, including high-eccentricity migration, allowing them to trace the primordial disk plane. In this context, we report measurements of the sky-projected stellar obliquity (λ) via the Rossiter–McLaughlin effect for two sub-Saturns in multiple-transiting systems: TOI-5126 b ($\lambda = 1 \pm 48^\circ$) and TOI-5398 b ($\lambda = -8.1^{+5.3}_{-6.3}^\circ$). Both are spin–orbit aligned, joining a fast-growing group of just three other compact sub-Saturn systems, all of which exhibit spin–orbit alignment. In aggregate with archival data, our results strongly suggest that sub-Saturn systems are primordially aligned and become misaligned largely in the postdisk phase, as appears to be the case increasingly for other exoplanet populations.

Unified Astronomy Thesaurus concepts: Exoplanet astronomy (486); Exoplanet dynamics (490); Exoplanet evolution (491); Extrasolar gaseous giant planets (509); Radial velocity (1332); Transits (1711)

Materials only available in the online version of record: data behind figure

1. Introduction

Stellar obliquity—i.e., the angle between the spin axis of the host star and the net orbit normal axis of the planets—is a powerful probe of a planetary system’s formation history. While the precise mechanisms driving spin–orbit misalignment are not yet clear, it is important to distinguish whether misalignment is largely a product of *high-eccentricity migration*, which should be confined to short-period isolated planets¹⁰ (e.g., hot Jupiters; see Dawson & Johnson 2018 and references therein), or some *universal process* that operates across planetary systems with a variety of architectures, e.g., magnetic warping (Lai et al. 2011; Romanova et al. 2013), interactions with stellar companions (Lubow & Ogilvie 2000; Batygin 2012), stellar flybys (Hao et al. 2013), or stellar gravity waves (Rogers et al. 2012, 2013).

Compact multiplanet systems may be critical to differentiate between these two scenarios, as their tight orbital configurations are inconsistent with high-eccentricity migration induced by planet–planet scattering (Rasio & Ford 1996; Chatterjee

et al. 2008), Lidov–Kozai cycling (Wu & Murray 2003; Fabrycky & Tremaine 2007; Naoz 2016), or secular interactions (Naoz et al. 2011; Wu & Lithwick 2011; Petrovich 2015), all of which tend to disrupt the orbits of nearby planetary neighbors (Mustill et al. 2015). As such, if high-eccentricity migration is the primary driver of misalignment, compact multiplanet systems will retain their primordially aligned configurations. On the other hand, if universal misalignment processes dominate, compact systems may be misaligned at a rate comparable to isolated systems.

The great majority of spin–orbit angle measurements have been made for close-in Jupiters, particularly hot Jupiters (see the recent review by Albrecht et al. 2022), which rarely host nearby companions (Steffen et al. 2012; Huang et al. 2016; Hord et al. 2021; Wu et al. 2023). Therefore, it is useful to expand the census of stellar obliquities to other types of exoplanets. Sub-Saturns, broadly defined as giant planets with masses ranging between that of Neptune ($\sim 17 M_\oplus$) and Saturn ($\sim 95 M_\oplus$), represent a particularly interesting population for such studies. The core accretion model implies that they are “failed gas giants” (Pollack et al. 1996), suggesting they have analogous origins to Jupiters (Dong et al. 2018; Lee 2019; Hallatt & Lee 2022). However, sub-Saturns are less amenable to detection than Jupiters and are relatively understudied as an exoplanet population, so few constraints on their formation histories exist. As of this writing, only about two dozen sub-Saturns have had their spin–orbit angle measured, demonstrating that these planets can take on a range of values

⁸ Flatiron Research Fellow.

⁹ 51 Pegasi b Fellow.

¹⁰ Planets that are single or have only distant planetary companion(s).



from near-perfect alignment to almost completely retrograde. However, only three of these measurements have been made for sub-Saturns in compact multiplanet systems: Kepler-9 b (Wang et al. 2018), AU Mic b (Hirano et al. 2020a), and WASP-148 b (Wang et al. 2022). While this sample is limited in number, all three systems show evidence of spin-orbit alignment and thus provide tentative support for primordial alignment.

The Transiting Exoplanets Survey Satellite (TESS) mission (Ricker et al. 2015), now well into its extended mission phase, has produced a growing sample of sub-Saturns around bright stars. Of particular interest to this work, TESS is responsible for the discovery of at least two sub-Saturns in compact multiplanet systems: TOI-5126 b (Fairnington et al. 2024) and TOI-5398 b (Mantovan et al. 2022, 2024a). Given the brightness of their host stars and advances in extreme precision radial velocity (RV), these systems are amenable to stellar obliquity measurements.

In this study, we present Rossiter–McLaughlin (RM) effect (Holt 1893; McLaughlin 1924; Rossiter 1924; Queloz et al. 2000) measurements for both confirmed compact TESS sub-Saturn systems, TOI-5126 and TOI-5398, using the high-precision NEID spectrograph (Schwab et al. 2016) on the WIYN 3.5 m telescope at Kitt Peak, AZ. TOI-5126, a relatively bright ($V = 10.1$ mag) late-type F dwarf ($T_{\text{eff}} = 6297$ K), hosts a hot sub-Saturn with a 5.5 day period and an outer warm sub-Neptune with a 17.9 day period (Fairnington et al. 2024). TOI-5398, a bright ($V = 10.1$ mag) early-type G dwarf ($T_{\text{eff}} = 6039$ K), harbors a warm sub-Saturn with a 10.6 day period and an inner hot sub-Neptune with a 4.8 day period (Mantovan et al. 2022, 2024a). Our reported spin-orbit angles for these two systems represent a significant contribution to the limited sample of sub-Saturns in compact multiplanet systems with such measurements. This work is additionally part of the 11th published outcome of the Stellar Obliquities in Long-period Exoplanet Systems survey, as detailed in a series of publications (Rice et al. 2021, 2022; Wang et al. 2022; Rice et al. 2023a, 2023b; Dong et al. 2023; Hixenbaugh et al. 2023; Lubin et al. 2023; Wright et al. 2023; Hu et al. 2024).

This paper is organized as follows. In Section 2, we outline our RV observations. In Section 3, we describe our determination of stellar parameters. In Section 4, we detail our modeling of the RM signals and, subsequently, the stellar obliquities. In Section 5, we quantify the significance of our results and discuss their implications for the origins of spin-orbit misalignment and the formation histories of sub-Saturns.

2. Observations

The RM effects of TOI-5126 and TOI-5398 were observed using the WIYN/NEID spectrograph in high resolution (HR) mode ($R \sim 110,000$; Halverson et al. 2016; Schwab et al. 2016) on 2023 February 28 and 2023 April 16, respectively. NEID is a fiber-fed (Kanodia et al. 2018), actively environmentally stabilized spectrograph (Stefansson et al. 2016; Robertson et al. 2019) with a wavelength coverage of 380–930 nm. For TOI-5126b, we obtain 20 RV measurements in HR mode with 1000 s exposures from 02:20 to 07:48 UT. In total, 14 of these RVs cover the full transit, while the remaining 6 provide an out-of-transit baseline, 1 occurring 0.3 hr preingress and the other 5 spanning nearly 1.5 hr postgress. These observations occurred under atmospheric conditions with a seeing range of $1''.2\text{--}2''.8$ (median $1''.75$) and an airmass range of $z = 1.03\text{--}2.31$. At a

wavelength of 5500 \AA , the NEID spectrograph achieved a signal-to-noise ratio (SNR) of 56 pixel^{-1} . For TOI-5398b, we obtain 14 RV measurements in HR mode with 1250 s exposures from 02:55 to 09:04 UT, 8 of which are in-transit, sampling nearly the entire transit (excluding ingress). The conditions featured a seeing range of $0''.7\text{--}1''.5$ (median $1''.0$) and an airmass range of $z = 1.08\text{--}1.71$. At the same wavelength, the spectrograph’s SNR was 60 pixel^{-1} . We obtain an additional 14 NEID RVs covering TOI-5398b’s orbit interspersed between 2022 April 8 and 2023 December 27, 4 with 240 s exposure times and 9 with 300 s exposure times, and we utilize these measurements in a subsequent global fit for this system.

The NEID spectra were analyzed using version 1.3.0 of the NEID Data Reduction Pipeline (NEID-DRP),¹¹ and RVs were derived via the cross-correlation function (CCF) method within NEID-DRP. We extracted the resulting barycentric-corrected RVs (denoted as CCFRVMOD within the NEID-DRP documentation) from the NExScI NEID Archive.¹² The RV data gathered from NEID for this study are illustrated in Figure 1 (note that we subtract the Keplerian baseline to more clearly demonstrate the RM effect) and are available through the Data Behind the Figure program (see the figure caption for the link).

3. Stellar Parameters

3.1. Synthetic Spectral Fit By *iSpec*

All out-of-transit NEID spectra for TOI-5126 and TOI-5398 are corrected for RV shifts, coadded, and subsequently utilized to determine the respective stellar atmospheric parameters, including stellar effective temperature (T_{eff}), surface gravity ($\log g_*$), metallicity ($[\text{Fe}/\text{H}]$), and projected rotational velocity ($v \sin i_*$). We use the synthetic spectral fitting technique provided by the Python package *iSpec* (Blanco-Cuaresma et al. 2014; Blanco-Cuaresma 2019) to measure these parameters.

We employ the SPECTRUM radiative transfer code (Gray & Corbally 1994), the MARCS atmosphere model (Gustafsson et al. 2008), and the sixth version of the GES atomic line list (Heiter et al. 2021), all integrated within *iSpec*, to create a synthetic model for all the combined out-of-transit NEID spectra (SNR of 112 for TOI-5126; SNR of 137 for TOI-5398). In our fitting process, we treat microturbulent velocities as a variable, allowing us to accurately represent the small-scale turbulent motions in the stellar atmosphere. Conversely, we determine macroturbulent velocities using an empirical relationship (Doyle et al. 2014) that leverages established correlations with various stellar attributes. We select specific spectral regions to streamline the fitting process, focusing on the wings of the $\text{H}\alpha$, $\text{H}\beta$, and Mg I triplet lines, which are indicative of T_{eff} and $\log g_*$, as well as Fe I and Fe II lines, which are crucial for constraining $[\text{Fe}/\text{H}]$ and $v \sin i_*$. We then utilize the Levenberg–Marquardt nonlinear least-squares fitting algorithm (Markwardt 2009) to refine our spectroscopic parameters by iteratively minimizing the χ^2 value between the synthetic and observed spectra. The final spectroscopic parameters are detailed in Table 1.

¹¹ Detailed information is available at: <https://neid.ipac.caltech.edu/docs/NEID-DRP/>.

¹² <https://neid.ipac.caltech.edu/>

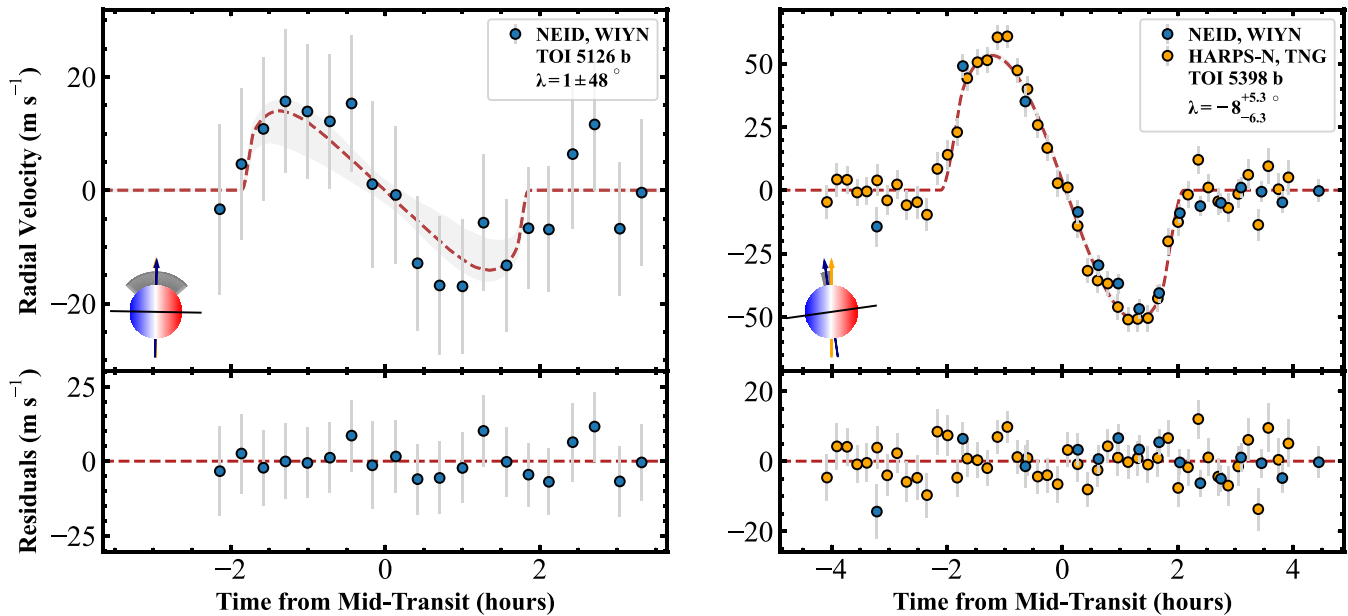


Figure 1. Keplerian signal-subtracted RVs (top panels) and RM model residuals (bottom panels) for TOI-5126 (left) and TOI-5398 (right). In the top panels, the best-fit RM models are shown with red dashed lines, and their uncertainties are indicated by gray shadows, while the planets’ spin-orbit configurations are depicted in the bottom-left portion of the plot. Note that the NEID RV measurement obtained ≈ 1 hr prior to ingress for TOI 5398b was taken on 2022 April 10 via 300 s exposure as part of our out-of-transit follow-up for this system. All NEID data used to generate this figure are available in a machine-readable format as the data behind the figure. (The data used to create this figure are available in the [online article](#).)

3.2. SED+MIST Fit By EXOFASTv2

To ascertain additional stellar parameters, such as stellar mass (M_*) and radius (R_*), we utilize the MESA Isochrones and Stellar Tracks (MIST) model (Choi et al. 2016; Dotter 2016) in combination with a spectral energy distribution (SED) fit. Photometry for the SED fit was compiled from various catalogs, including 2MASS (Cutri et al. 2003), WISE (Cutri et al. 2021), TESS (Ricker et al. 2015), and Gaia DR3 (Gaia Collaboration et al. 2023). We apply Gaussian priors based on our synthetic spectral fit to T_{eff} and $[\text{Fe}/\text{H}]$, along with the parallax from Gaia DR3 and an upper limit for the V -band extinction from Schlafly & Finkbeiner 2011. To accommodate the approximate 2.4% systematic uncertainty floor in T_{eff} , as suggested by Tayar et al. (2022), we increase the uncertainties of T_{eff} to 150 K for both TOI-5126 and TOI-5398.

As mentioned in Fairmington et al. (2024) and Mantovan et al. (2024a), respectively, both TOI-5126 and TOI-5398 exhibit strong stellar rotation signals, providing additional stringent constraints on their stellar ages. We adopt Equation (7) from Barnes (2007) to calculate the gyrochronological ages for these stars based on the stellar rotation periods derived from our work (see Section 4). The resulting gyrochronological ages for TOI-5126 and TOI-5398 are 0.13 ± 0.02 and $0.42_{-0.05}^{+0.07}$ Gyr, respectively. Subsequently, we adopt these ages and their 3σ uncertainties as priors for the stellar ages in our SED fit.

We perform the SED fitting using the Differential Evolution Markov Chain Monte Carlo (DEMC) technique, integrated within EXOFASTv2 (Eastman 2017; Eastman et al. 2019), from which we obtain uncertainty estimates. The DEMCMC procedure was considered converged when the Gelman–Rubin diagnostic (\hat{R} ; Gelman & Rubin 1992) fell below 1.01 and the count of independent draws surpassed 1000. Our final adopted stellar parameters are listed in Table 1; we find all derived values are consistent (within $<2\sigma$) with results from discovery

papers (see Fairmington et al. 2024 for TOI-5126, Mantovan et al. 2024a for TOI-5398).

4. Obliquity Modeling

We determine the sky-projected spin-orbit angle λ for TOI-5126b and TOI-5398b by jointly fitting the transit photometry from their respective discovery papers (including 2 minute cadence TESS light curves) and all in-transit and out-of-transit RVs from our NEID observations (see Section 2) using a modified version of the *allesfitter* package (Günther & Daylan 2021). The modified version of *allesfitter* incorporates the Hirano et al. (2011) RM model implemented in *tracit* (Hjorth et al. 2021; Knudstrup & Albrecht 2022). We exclude the transit data for the non-sub-Saturn planet in both systems but model their RVs (TOI-5126c at $P = 17.9$ days and TOI-5398c at $P = 4.77$ days).

For TOI-5126b, we adopt the Presearch Data Conditioning Simple Aperture Photometry (PDCSAP) light curves from the TESS Science Processing Operations Center, modeling eight full transits and one partial transit from Sector 45, four full transits and one partial transit from Sector 46, and four full transits from Sector 48. Within *allesfitter*, we simultaneously fit the TESS and NEID data together with all photometric data utilized in TOI-5126b’s discovery paper (Fairmington et al. 2024), including observations from the Characterising Exoplanets Satellite (Benz et al. 2021) as well as ground-based 1.0 m telescopes at McDonald Observatory in Fort Davis, TX, and at the Cerro Tololo Inter-American Observatory (CTIO) in Cerro Tololo, Chile, which are both part of the Las Cumbres Observatory Global Network (LCOGT; Brown et al. 2013). Due to their large scatter relative to the expected planetary RV semi-amplitudes, we do not make use of the out-of-transit RVs presented in Fairmington et al. (2024), which were obtained from the Tillinghast Reflector Echelle Spectrograph at the Fred Lawrence Whipple Observatory

Table 1
Stellar and Planetary Parameters of TOI-5126 and TOI-5398

| Description | | Priors ^a | TOI-5126 ^b | Priors ^a | TOI-5398 |
|------------------------------------|--|--------------------------------------|-------------------------------------|--------------------------------------|--------------------------------|
| Stellar Parameters: | | | | | |
| Synthetic spectral fit: | | | | | |
| T_{eff} | Effective temperature (K) | ... | 6256 ± 87 | ... | 6072 ± 89 |
| [Fe/H] | Metallicity (dex) | ... | 0.03 ± 0.07 | ... | 0.01 ± 0.05 |
| $\log g_*$ | Surface gravity ($\log_{10}(\text{cm s}^{-2})$) | ... | 4.39 ± 0.20 | ... | 4.63 ± 0.16 |
| SED+MIST fit (adopted): | | | | | |
| M_* | Stellar mass (M_{\odot}) | ... | $1.248_{-0.034}^{+0.035}$ | ... | 1.105 ± 0.029 |
| R_* | Stellar radius (R_{\odot}) | ... | 1.199 ± 0.033 | ... | 1.035 ± 0.028 |
| T_{eff} | Effective temperature (K) | $\mathcal{N}(6256 6256, 150)$ | 6297_{-86}^{+88} | $\mathcal{N}(6072 6072, 150)$ | 6039_{-81}^{+80} |
| [Fe/H] | Metallicity (dex) | $\mathcal{N}(0.03 0.03, 0.07)$ | $0.056_{-0.065}^{+0.068}$ | $\mathcal{N}(0.01 0.01, 0.05)$ | $0.014_{-0.049}^{+0.050}$ |
| $\log g_*$ | Surface gravity ($\log_{10}(\text{cm s}^{-2})$) | ... | 4.377 ± 0.019 | ... | $4.451_{-0.019}^{+0.020}$ |
| Age | Age (Gyr) | $\mathcal{N}(0.13 0.13, 0.06)$ | $0.170_{-0.049}^{+0.059}$ | $\mathcal{N}(0.42 0.42, 0.21)$ | $0.54_{-0.17}^{+0.20}$ |
| ϖ | Parallax (mas) | $\mathcal{N}(6.257 6.257, 0.024)$ | $6.256_{-0.026}^{+0.025}$ | $\mathcal{N}(7.648 7.648, 0.017)$ | 7.649 ± 0.018 |
| d | Distance (pc) | ... | $159.84_{-0.65}^{+0.66}$ | ... | $130.74_{-0.31}^{+0.30}$ |
| $v \sin i_*$ ($\pm \text{Spec}$) | Projected stellar rotational velocity (km s^{-1}) | ... | 13.84 ± 0.80 | ... | 7.65 ± 0.54 |
| ... | ... | ... | ... | ... | ... |
| RM Parameters: | | | | | |
| λ | Sky-projected spin-orbit angle (deg) | $\mathcal{U}(0 -180, 180)$ | 1 ± 48 | $\mathcal{U}(0 -180, 180)$ | $-8.1_{-6.3}^{+5.3}$ |
| $v \sin i_*$ | Projected stellar rotational velocity (km s^{-1}) | $\mathcal{N}(13.84 13.84, 0.80)$ | 13.77 ± 0.79 | $\mathcal{N}(7.65 7.65, 0.54)$ | 7.58 ± 0.19 |
| ... | ... | ... | ... | ... | ... |
| ξ | Microturbulent velocity (km s^{-1}) | $\mathcal{T}(1.23 1.23, 1, 0, 10)$ | $1.37_{-0.81}^{+0.93}$ | $\mathcal{T}(1.14 1.14, 1, 0, 10)$ | $1.20_{-0.68}^{+0.74}$ |
| ζ | Macroturbulent velocity (km s^{-1}) | $\mathcal{T}(4.52 4.52, 1, 0, 10)$ | 4.57 ± 0.98 | $\mathcal{T}(3.77 3.77, 1, 0, 10)$ | 3.63 ± 0.75 |
| Planetary Parameters: | | | | | |
| R_b/R_* | Planet-to-star radius ratio | $\mathcal{U}(0.0348 0, 1)$ | 0.03612 ± 0.00042 | $\mathcal{U}(0.0898 0, 1)$ | 0.09116 ± 0.00059 |
| $(R_* + R_b)/a_b$ | Ratio of the sum of star and planet radii to semimajor axis | $\mathcal{U}(0.0916 0, 1)$ | $0.08951_{-0.00078}^{+0.0015}$ | $\mathcal{U}(0.0543 0, 1)$ | $0.05295_{-0.00080}^{+0.0010}$ |
| ... | ... | ... | ... | ... | ... |
| $\cos i_b$ | Cosine of inclination | $\mathcal{U}(0.0 0, 1)$ | $0.0097_{-0.0067}^{+0.0091}$ | $\mathcal{U}(0.0 0, 1)$ | $0.0103_{-0.0046}^{+0.0040}$ |
| $T_{0:b}$ | Mid-transit time—2459600 (BJD _{TDB}) | $\mathcal{U}(27.039 26.939, 27.139)$ | $27.03719_{-0.00043}^{+0.00053}$ | $\mathcal{U}(16.492 16.392, 16.592)$ | 16.49202 ± 0.00022 |
| P_b | Orbital period (days) | $\mathcal{U}(5.458 5.358, 5.558)$ | $5.4588627_{-0.000085}^{+0.000077}$ | $\mathcal{U}(10.591 10.491, 10.691)$ | 10.590535 ± 0.000024 |
| K_b | RV semiamplitude (m s^{-1}) | $\mathcal{N}(6.6 6.6, 2.5)$ | 6.6 ± 2.5 | $\mathcal{N}(15.7 15.7, 1.5)$ | 15.2 ± 1.3 |
| $q_{1:\text{NEID}}$ | Linear limb-darkening coefficient for NEID | $\mathcal{U}(0.5 0, 1)$ | 0.51 ± 0.34 | $\mathcal{U}(0.5 0, 1)$ | $0.31_{-0.22}^{+0.35}$ |
| $q_{2:\text{NEID}}$ | Quadratic limb-darkening coefficient for NEID | $\mathcal{U}(0.5 0, 1)$ | 0.46 ± 0.31 | $\mathcal{U}(0.5 0, 1)$ | $0.17_{-0.12}^{+0.33}$ |
| $q_{1:\text{HARPS-N}}$ | Linear limb-darkening coefficient for HARPS-N | ... | ... | $\mathcal{U}(0.5 0, 1)$ | $0.873_{-0.15}^{+0.089}$ |
| $q_{2:\text{HARPS-N}}$ | Quadratic limb-darkening coefficient for HARPS-N | ... | ... | $\mathcal{U}(0.5 0, 1)$ | 0.381 ± 0.091 |
| Derived Parameters: | | | | | |
| M_b | Planetary mass (M_J) | ... | 0.067 ± 0.026 | ... | 0.135 ± 0.043 |
| R_b | Planetary radius (R_J) | ... | 0.421 ± 0.014 | ... | 0.921 ± 0.026 |
| a_b/R_* | Semimajor axis scaled by stellar radius | ... | $11.57_{-0.18}^{+0.10}$ | ... | $20.61_{-0.39}^{+0.31}$ |
| a_b | Semimajor axis (au) | ... | 0.0644 ± 0.0020 | ... | 0.0994 ± 0.0032 |
| i_b | Inclination (deg) | ... | $89.44_{-0.51}^{+0.39}$ | ... | $89.41_{-0.23}^{+0.26}$ |
| $T_{14:b}$ | Total transit duration (hr) | ... | $3.711_{-0.020}^{+0.022}$ | ... | 4.205 ± 0.017 |
| $u_{1:\text{NEID}}$ | Linear limb-darkening coefficient for NEID | ... | $0.56_{-0.38}^{+0.57}$ | ... | $0.162_{-0.099}^{+0.22}$ |
| $u_{2:\text{NEID}}$ | Quadratic limb-darkening coefficient for NEID | ... | 0.04 ± 0.42 | ... | $0.32_{-0.32}^{+0.36}$ |
| $u_{1:\text{HARPS-N}}$ | Linear limb-darkening coefficient for HARPS-N | ... | ... | ... | 0.70 ± 0.17 |
| $u_{2:\text{HARPS-N}}$ | Quadratic limb-darkening coefficient for HARPS-N | ... | ... | ... | 0.22 ± 0.17 |
| GP Parameters: | | | | | |
| $\ln B_{\text{NEID}}$ | Amplitude scaling factor | ... | ... | $\mathcal{U}(0 -10, 10)$ | $-6.65_{-0.63}^{+0.53}$ |
| $\ln C_{\text{NEID}}$ | Balance factor | ... | ... | $\mathcal{U}(0 -10, 10)$ | $-1.0_{-7.2}^{+8.2}$ |

Table 1
(Continued)

| | Description | Priors ^a | TOI-5126 ^b | Priors ^a | TOI-5398 |
|------------------------------|--------------------------|---------------------|-----------------------|-------------------------|-------------------------|
| $\ln L_{\text{NEID}}$ | Coherence timescale | ... | ... | $\mathcal{U}(0-10, 10)$ | $-1.0^{+4.6}_{-7.1}$ |
| $\ln P_{\text{rot,NEID}}$ | Stellar rotation period | ... | ... | $\mathcal{N}(2 2, 0.2)$ | 2.02 ± 0.18 |
| $\ln B_{\text{HARPS-N}}$ | Amplitude scaling factor | ... | ... | $\mathcal{U}(0-10, 10)$ | -7.17 ± 0.15 |
| $\ln C_{\text{HARPS-N}}$ | Balance factor | ... | ... | $\mathcal{U}(0-10, 10)$ | $-0.9^{+8.3}_{-7.3}$ |
| $\ln L_{\text{HARPS-N}}$ | Coherence timescale | ... | ... | $\mathcal{U}(0-10, 10)$ | $-1.15^{+0.62}_{-0.96}$ |
| $\ln P_{\text{rot,HARPS-N}}$ | Stellar rotation period | ... | ... | $\mathcal{N}(2 2, 0.2)$ | 2.01 ± 0.18 |

Notes.

^a The notations $\mathcal{U}(p_0|a, b)$, $\mathcal{N}(p_0|\mu, \sigma)$, and $\mathcal{T}(p_0|\mu, \sigma, a, b)$ represent the uniform, Gaussian, and truncated Gaussian distributions, respectively. Here, p_0 denotes the initial guess, a and b the lower and upper bounds, respectively, μ the median value, and σ the standard deviation.

^b For TOI-5126b, we adopt the results of Fairmington et al. (2024) as priors for our fitted RV semi-amplitude K_b , and we directly adopt their planetary mass estimate M_b , which was obtained via the Otegi et al. (2020) mass–radius relation.

(FLWO) and the CHIRON spectrograph on the SMARTS telescope at CTIO.

For TOI-5398b, we also consider the PDCSAP TESS light curves (we did not find substantive evidence for the over-corrections in the PDCSAP data reported by Mantovan et al. 2024a), modeling two full transits from TESS Sector 48, as well as photometry from the LCOGT 1.0 m telescopes at McDonald Observatory and Teide Observatory and from the 1.2 m KeplerCam at FLWO on Mount Hopkins, AZ (all sourced from Mantovan et al. 2024a). We additionally incorporate the out-of-transit RVs from Mantovan et al. (2024a), which were obtained from the High Accuracy Radial velocity Planet Searcher (HARPS-N, Cosentino et al. 2012) at the Italian Telescopio Nazionale Galileo. Recently, Mantovan et al. (2024b) published an independent RM effect measurement of TOI-5398b; therefore, we model the RM effect for this target both with and without the inclusion of their published in-transit RVs (holding all other factors equal), which were also obtained from the HARPS-N spectrograph.¹³ To account for strong stellar activity in the RVs, we apply a rotational Gaussian process (GP) regression kernel formulated by Foreman-Mackey et al. (2017),

$$k(\tau) = \frac{B}{2 + C} e^{-\tau/L} \left[\cos\left(\frac{2\pi\tau}{P_{\text{rot}}}\right) + (1 + C) \right] \quad (1)$$

where P_{rot} represents the period of stellar rotation, L denotes the coherence timescale, τ signifies the interval between two successive data points, B is a scaling hyperparameter that adjusts the amplitude, and C serves as the balance parameter for the periodic and nonperiodic components of the GP kernel. For TOI-5398, we note that our adopted GP model is most similar to “Case 1” from Mantovan et al. (2024a), though the results from their multidimensional “Case 3” were ultimately adopted.

For both TOI-5126b and TOI-5398b, we adopt priors but utilize the results reported in the literature (Fairmington et al. 2024 and Mantovan et al. 2024a, respectively) as our initial guesses for R_p/R_* , $(R_* + R_p)/a$, $\cos(i)$, T_0 , P , and K (see Table 1 for parameter definitions). We fixed eccentricity (e) and the argument of periastron (ω) to 0 due to the near-zero eccentricity reported by the discovery papers of TOI-5126b and TOI-5398b. We consider transformed linear and quadratic

limb-darkening coefficients q_1 and q_2 , in addition to physical linear and quadratic limb-darkening coefficients u_1 and u_2 ,¹⁴ for both NEID and HARPS-N, initializing q_1 and q_2 at 0.5 for each instrument. As an initial guess for $v \sin i_*$, for which we apply Gaussian priors, we adopt the values derived from our synthetic spectral fit. Finally, we initialize λ at 0° for both systems. All parameters (except e and ω) are allowed to vary during the fitting process. To account for the short-term overnight instrumental systematics and stellar variability in the RM fit, we employ a quadratic baseline for TOI-5126 and a constant baseline for TOI-5398, though we note that all tested baselines (constant, linear, quadratic, and cubic) produced consistent λ values (within 1σ).

For the fits of both systems, we sample the posterior distributions for all modeled parameters using an affine-invariant Markov Chain Monte Carlo (MCMC) grounded in emcee (Foreman-Mackey et al. 2013) with 100 walkers. Best-fit parameters were obtained after 200,000 accepted steps per walker were reached (note that each ran 10,000 burner steps); our final MCMC results and associated 1σ uncertainties are summarized in Table 1. Additionally, all Markov Chains reached $>50\times$ their autocorrelation lengths, indicating convergence.

We find good agreement ($<2\sigma$ difference) with all stellar, planetary, and derived parameters reported in the discovery papers of both systems (Fairmington et al. 2024 for TOI-5126b and Mantovan et al. 2024a for TOI-5398b), except $T_{0;b}$ (2.5σ discrepant) for TOI-5126, which may be due to tentative transit timing variations (see Fairmington et al. 2024). Critically, our RM fits show that both sub-Saturns are consistent with spin-orbit alignment. For TOI-5126b, we find a best-fit projected obliquity of $\lambda = 1 \pm 48^\circ$. For TOI-5398b, we compute a best-fit $\lambda = -8.1^{+5.3}_{-6.3}^\circ$ using in-transit RVs from both NEID (presented in this work) and HARPS-N (presented in Mantovan et al. 2024b), while we derive a marginally aligned value of $\lambda = -24^{+14}_{-13}^\circ$ using our NEID data alone (note that both values are within 2σ of the $\lambda = 3.0^{+6.8}_{-4.2}$ reported by Mantovan et al. 2024b). Figure 1 reveals the best-fit joint models and associated residuals for both systems, while Table 1 contains all fitted and derived parameters.

It is useful to additionally measure the 3D stellar obliquity ψ , which yields a system’s true spin-orbit configuration. To estimate

¹³ Our work was otherwise prepared concurrently and independently to that of Mantovan et al.

¹⁴ The relationship between the transformed (q_1, q_2) and physical (u_1, u_2) limb-darkening coefficients is described in Kipping (2013) by Equation (15): $u_1 = 2\sqrt{q_1} q_2$ and Equation (16): $u_2 = \sqrt{q_1}(1 - 2q_2)$.

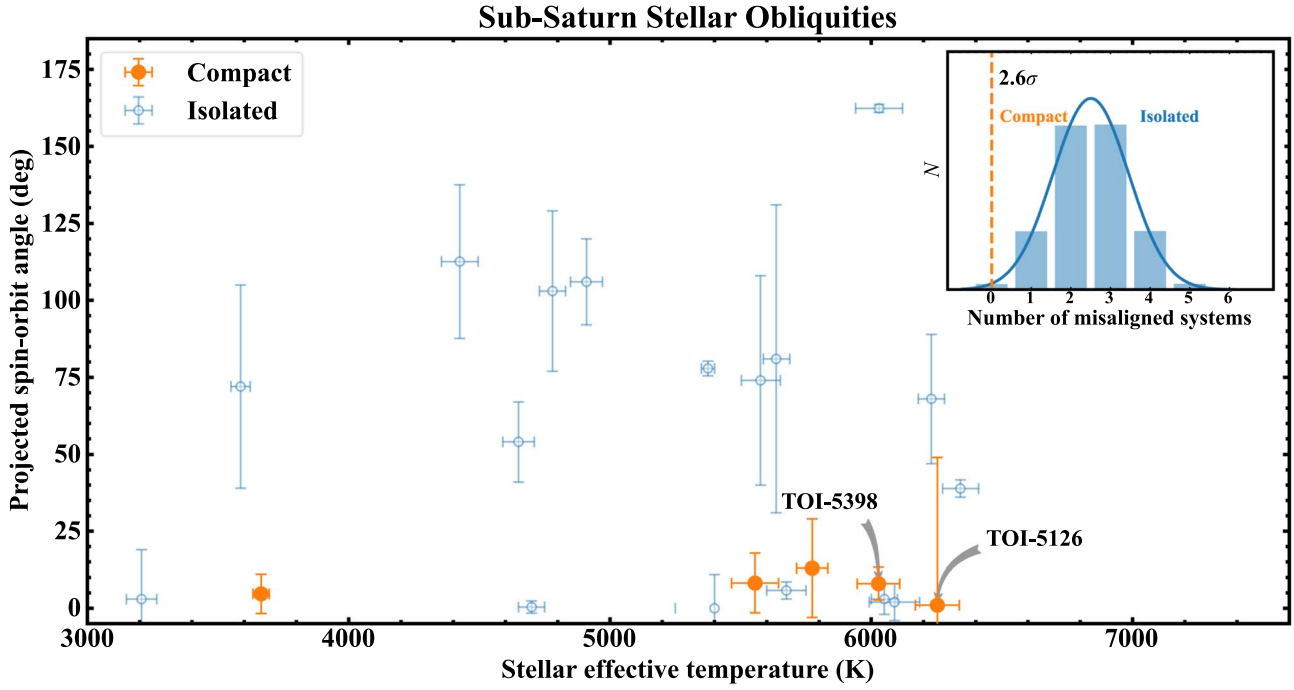


Figure 2. Sky-projected stellar obliquity λ vs. stellar effective temperature T_{eff} for all sub-Saturns considered in this work, with 1σ error bars shown. The subpanel in the top right displays the resultant distributions of the number of misaligned sub-Saturns found in compact multiplanet systems (dashed line) and the number of misaligned isolated sub-Saturns after performing 100,000 random draws (bars), with statistical significance (2.6σ) indicated. In both panels, orange corresponds to sub-Saturns in compact multiplanet systems, while blue corresponds to isolated sub-Saturns.

ψ , we first derive the stellar inclination i_* and stellar equatorial velocity v_{eq} for both TOI-5126 and TOI-5398 by applying the Bayesian inference method presented by Masuda & Winn (2020) and Hjorth et al. (2021) to our values for stellar radius R_* , stellar rotation period P_{rot} , and $\cos i_*$. We utilize the aforementioned TESS PDCSAP light curves to compute the stellar rotation periods for each target, employing the autocorrelation function (ACF) implemented in *SpinSpotter* (Holcomb et al. 2022). Correspondingly, we find $P_{\text{rot}} = 4.05 \pm 0.21$ days for TOI-5126 and $P_{\text{rot}} = 7.443 \pm 0.041$ days for TOI-5398. However, due to the effects of latitudinal differential rotation (Epstein & Pinsonneault 2014; Aigrain et al. 2015) and the systematic uncertainty floor (of $\approx 4.2\%$) on the derivation of stellar radii (Tayar et al. 2022), we adopt a 10% uncertainty floor on our derived stellar rotation periods, yielding $P_{\text{rot}} = 4.05 \pm 0.41$ days and $P_{\text{rot}} = 7.443 \pm 0.74$ days for TOI-5126 and TOI-5398, respectively. These estimates are consistent with those reported by their respective discovery papers, which both applied the Lomb–Scargle periodogram to photometric data, rather than the ACF, in order to ascertain their adopted rotation periods (Fairmington et al. 2024 find $P_{\text{rot}} = 4.602^{+0.071}_{-0.067}$ days for TOI-5126, while Mantovan et al. 2024a find $P_{\text{rot}} = 7.34 \pm 0.05$ days for TOI-5398). From our Bayesian analysis, we find $i_* = 90^\circ \pm 15^\circ$ and $v_{\text{eq}} = 14.36 \pm 1.02 \text{ km s}^{-1}$ for TOI-5126 and $i_* = 91^\circ \pm 17^\circ$ and $v_{\text{eq}} = 8.09 \pm 0.87 \text{ km s}^{-1}$ for TOI-5398 and compute the true 3D stellar obliquities as (see Equation (9) of Fabrycky & Winn 2009)

$$\cos \psi = \cos i_* \cos i + \sin i_* \sin i \cos \lambda, \quad (2)$$

where i is the inclination angle of the planet. For TOI-5126b, we find a true obliquity of $\psi = 37.1^{+20.3}_{-33.6}^\circ$. Similarly, we derive $\psi = 16.4^{+7.6}_{-10.3}^\circ$ for TOI-5398b (in good agreement with the $\psi = 13.2 \pm 8.2$ derived by Mantovan et al. 2024b), demonstrating that both systems are consistent with alignment.

5. Discussion

While sub-Saturns broadly appear to boast a wide range of stellar obliquities, the few previously confirmed to be in compact multiplanet systems are exclusively aligned. Our RM measurements for two of such recently confirmed sub-Saturns, TOI-5126b and TOI-5398b, continue this trend, as both are consistent with alignment. We show the updated stellar obliquity distribution for the sub-Saturn population as a function of stellar effective temperature in Figure 2. To construct this sub-Saturn sample, we combine the catalogs of Albrecht et al. (2022) and TEPcat¹⁵ (Southworth 2011) accessed on 2024 March 7. We consider only RM effect measurements, which exhibit near-uniform sensitivity to the full range of possible λ values (compared to nonuniform methods such as starspot tracking or gravity darkening; Dong & Foreman-Mackey 2023; Siegel et al. 2023) and constitute the majority of obliquity measurements (Triaud 2018; Albrecht et al. 2022), prioritizing those selected in Albrecht et al. (2022; we otherwise adopt the “preferred” measurements from TEPcat). Finally, we apply a mass cut of $17 M_{\oplus} < M_{pl} < 95 M_{\oplus}$ and select only single-star systems by cross-matching our sample with the multistar catalog of Rice et al. (2024), which is based on the most recent data from Gaia DR3. This yields 22 sub-Saturn systems with λ measurements to comprise our statistical sample. We further distinguish between sub-Saturns that are isolated and those in compact multiplanet systems, which we define as having a nearby companion with a period ratio of < 4 . All sub-Saturns considered in this work are presented in Table 2 (note that we supplement any missing parameters using the NASA Exoplanet Archive¹⁶ and values adopted by their respective λ reference papers). Our RM measurements allow for more reliable

¹⁵ <https://www.astro.keele.ac.uk/jkt/tepcat/obliquity.html>

¹⁶ <https://exoplanetarchive.ipac.caltech.edu>

Table 2
Sub-Saturns around Single Stars With a Stellar Obliquity Measurement

| System | Planet | T_{eff} (K) | M_* [M_{\odot}] | P (days) | M_{pl} (M_{\oplus}) | λ ($^{\circ}$) | λ Reference |
|-------------------------------------|--------|----------------------|----------------------------|----------------------------------|----------------------------|---------------------------|--------------------------------|
| Compact Multiplanet Systems: | | | | | | | |
| AU Mic | b | 3665±100 | 0.5±0.03 | 8.46±0.0000052 | 20.12 $^{+1.57}_{-1.72}$ | -4.7 $^{+6.4}_{-6.8}$ | Hirano et al. (2020a) |
| Kepler-9 | b | 5774±60 | 1.02 $^{+0.03}_{-0.04}$ | 19.24±0.00006 | 43.41 $^{+1.6}_{-2.0}$ | 13±16 | Wang et al. (2018) |
| WASP-148 | b | 5555±21 | 0.95 $^{+0.03}_{-0.05}$ | 8.80±0.000043 | 91.24 $^{+6.99}_{-5.09}$ | -8.2 $^{+9.7}_{-8.7}$ | Wang et al. (2022) |
| TOI-5126 | b | 6297 $^{+88}_{-86}$ | 1.248 $^{+0.035}_{-0.034}$ | 5.46±0.0000062 | 21 $^{+9}_{-7}$ | 1±48 | This work |
| TOI-5398 | b | 6039 $^{+80}_{-81}$ | 1.105±0.029 | 10.59 $^{+0.000041}_{-0.000046}$ | 42.9±13.7 | -8.1 $^{+5.3}_{-6.3}$ | This work |
| Isolated Systems: | | | | | | | |
| GJ 436 | b | 3586±54 | 0.47±0.07 | 2.64±0.00000057 | 22.25±2.23 | 72 $^{+33}_{-24}$ | Bourrier et al. (2018) |
| HAT-P-11 | b | 4780±50 | 0.81 $^{+0.02}_{-0.03}$ | 4.89±0.0000068 | 26.7±2.23 | 103 $^{+26}_{-10}$ | Winn et al. (2010b) |
| HAT-P-12 | b | 4650±45 | 0.73±0.02 | 3.21±0.0000021 | 67.08±3.81 | -54 $^{+41}_{-13}$ | Mancini et al. (2018) |
| HD 89345 | b | 5576 $^{+70}_{-71}$ | 1.16 $^{+0.04}_{-0.05}$ | 11.81±0.0002 | 34.97 $^{+5.4}_{-5.72}$ | 74.2 $^{+33.6}_{-32.5}$ | Bourrier et al. (2023) |
| HD 332231 | b | 6089 $^{+97}_{-96}$ | 1.13±0.08 | 18.71±0.00043 | 77.57±6.68 | -2±6 | Knudstrup & Albrecht (2022) |
| HIP 67522 | b | 5675±75 | 1.22±0.05 | 6.96 $^{+0.000016}_{-0.000015}$ | 79 ^a | -5.8 $^{+2.8}_{-5.7}$ | Heitzmann et al. (2021) |
| K2-25 | b | 3207±58 | 0.26±0.01 | 3.48 $^{+0.000006}_{-0.000005}$ | 24.51 $^{+5.7}_{-5.2}$ | 3±16 | Stefansson et al. (2020) |
| K2-105 | b | 5636±70 | 1.05±0.02 | 8.27 $^{+0.000007}_{-0.0000067}$ | 30.01±19.0 | -81 $^{+50}_{-47}$ | Bourrier et al. (2023) |
| KELT-11 | b | 5375±25 | 1.44±0.07 | 4.74±0.00003 | 54.36±4.77 | -77.86 $^{+2.36}_{-2.26}$ | Mounzer et al. (2022) |
| TOI-1842 | b | 6230±50 | 1.46±0.03 | 9.57 $^{+0.0002}_{-0.0001}$ | 68.03 $^{+12.72}_{-12.08}$ | -68.1 $^{+21.7}_{-14.7}$ | Hixenbaugh et al. (2023) |
| TOI-1859 | b | 6341 $^{+68}_{-70}$ | 1.29±0.06 | 63.48±0.0001 | 68.67 ^a | 38.9 $^{+2.8}_{-2.7}$ | Dong et al. (2023) |
| WASP-39 | b | 5400±50 | 0.93±0.03 | 4.06±0.000009 | 89.01±9.54 | 0±11 | Mancini et al. (2018) |
| WASP-69 | b | 4700±50 | 0.98±0.14 | 3.87±0.000002 | 92.19±9.54 | 0.4 $^{+2.0}_{-1.9}$ | Casasayas-Barris et al. (2017) |
| WASP-107 | b | 4425±70 | 0.68±0.02 | 5.72±0.000002 | 30.52±1.59 | 118.1 $^{+37.8}_{-19.1}$ | Rubenzahl et al. (2021) |
| WASP-131 | b | 6030±50 | 1.06±0.06 | 5.32±0.000005 | 85.83±6.36 | 162.4 $^{+1.3}_{-1.2}$ | Doyle et al. (2023) |
| WASP-156 | b | 4910±61 | 0.84±0.05 | 3.84±0.000003 | 40.69 $^{+3.18}_{-2.86}$ | 105.7 $^{+14.0}_{-14.4}$ | Bourrier et al. (2023) |
| WASP-166 | b | 6050±50 | 1.19±0.06 | 5.44±0.000004 | 32.11±1.59 | 3±5 | Hellier et al. (2019) |

Note.

^a Calculated using the Chen & Kipping (2017) mass–radius relationship.

statistical analyses to be performed on the relationship between compact configurations and spin–orbit alignment for sub-Saturns (Section 5.1) and thus more robust constraints on the origins of spin–orbit misalignment as well as the formation histories of the sub-Saturn population (Sections 5.2 and 5.3).

5.1. Sub-Saturns in Compact Multiplanet Systems Are Significantly Aligned

It is clear from Figure 2 that spin–orbit alignment is much more common for sub-Saturns in compact multiplanet systems than for isolated sub-Saturns, while no clear relation exists for the host star’s effective temperature (as seen in previous works, e.g., Albrecht et al. 2022). Our two stellar obliquity measurements increase the sample of sub-Saturns in compact configurations to five, enabling the first statistical tests of this trend. We investigate the statistical significance of preferential alignment in compact systems by comparing the number of misaligned systems found in the compact multiplanet sub-Saturn sample (zero) with that found in a series of random draws from the isolated sub-Saturn sample. We perform this statistical analysis using the projected 2D spin–orbit angles λ , rather than the true 3D spin–orbit angles ψ , for two reasons: (i) considering solely ψ is statistically prohibitive, as only 14 of the 22 systems in our sample have ψ measurements, and (ii) nearly all 22 systems in our sample orbit cooler stars ($T_{\text{eff}} < 6250$ K), which tend to have edge-on inclinations such that $\psi \approx |\lambda|$ (see Louden et al. 2021; note that the average difference between ψ and $|\lambda|$ is just 13 $^{\circ}$ for the 14 systems with measurements for both angles).

Of the 22 sub-Saturns with λ measurements considered in this work, 5 are in compact multiplanet systems, while the other 17 are isolated. Of the 5 in compact configurations, none are misaligned, while 9/17 (53%) isolated sub-Saturns are misaligned. We define misalignment as $|\lambda| > 10^{\circ}$ at the 1σ level (i.e., $|\lambda| - \sigma_{\lambda} > 10^{\circ}$) and $\lambda > 0^{\circ}$ at the 2σ level (i.e., $|\lambda| - 2\sigma_{\lambda} > 0^{\circ}$), where we adopt the 1σ uncertainties (σ_{λ}) reported for each λ measurement (see Table 2). In order to perform a fair comparison between the compact multiplanet sample and the isolated sample, we randomly select and classify the alignment of 5 isolated sub-Saturns. We perform 100,000 iterations of these random draws, counting the number of misaligned systems for each, and fit a Gaussian function over the resulting distribution of N systems per count. The upper-right subpanel of Figure 2 reveals the result, illustrating that sub-Saturns in compact multiplanet systems are more often aligned than isolated sub-Saturns to a significance level of 2.6σ .

We verified that this significance is robust to the precise misalignment criteria adopted by rerunning the above procedure with the following alternative cuts: $\lambda > 15^{\circ}$ and $\lambda > 0^{\circ}$ at the 2σ level (2.6σ significance), (ii) $\lambda > 20^{\circ}$ and $\lambda > 0^{\circ}$ at the 2σ level (2.6σ significance), (iii) $\lambda > 15^{\circ}$ (2.3σ significance), and (iv) $\lambda > 20^{\circ}$ (2.3σ significance). Assuming our original alignment criteria, we additionally vary the Neptune/sub-Saturn mass boundary and rerun our procedure: (i) $15 M_{\oplus}$ (3.0σ significance) and (ii) $0.1 M_J$ (1.8σ significance). We note that while the significance appears to degrade with an increasing mass bound, this trend is likely not astrophysical, as the significance is directly proportional to the number of sub-

Saturns in compact systems considered, which drops from six assuming a $15 M_{\oplus}$ bound to only three assuming a $0.1 M_J$ ($\approx 32 M_{\oplus}$) bound. Finally, we note that the young (~ 20 Myr), aligned, compact sub-Saturn system AU Mic still hosts a dusty debris disk (Hirano et al. 2020a; Plavchan et al. 2020), meaning that its spin-orbit angle and compactness has likely not yet had the opportunity to be affected by various pathways to trigger postdisk eccentric migration (Wu et al. 2023). Therefore, while this system provides strong support for primordial alignment, it may bias our statistical test; we rerun our original procedure excluding AU Mic (such that there are only four compact sub-Saturn systems) and find that the significance is maintained but reduced to 2.2σ .

5.2. Evidence for Primordial Alignment and Misalignment via Eccentric Migration

In this work, we have demonstrated that sub-Saturns in compact planetary systems are significantly more aligned than those without nearby planetary companions (at the 2.6σ level). This trend of spin-orbit alignment in compact multiplanet systems around single stars is not limited to sub-Saturns, however. Short-period ($P \lesssim 100$ days) Jupiters provided the first robust evidence for this phenomenon. Specifically, all measured spin-orbit angles for short-period Jupiters with nearby companions, even hot Jupiters, are consistent with alignment, e.g., Kepler-30 (Sanchis-Ojeda et al. 2012), Kepler-89 (Albrecht et al. 2013), WASP-47 (Sanchis-Ojeda et al. 2015), TOI-1478 (Rice et al. 2022), TOI-2202 (Rice et al. 2023b), and TOI-1670 (Lubin et al. 2023). Conversely, isolated short-period Jupiters display a wide range of obliquities and are frequently misaligned (Albrecht et al. 2012, 2022). While there is a paucity of spin-orbit measurements for sub-Neptunes and super-Earths, most of these lower-mass planets reside in compact multiplanet systems, and those with secure obliquity measurements are aligned, e.g., Kepler-50, Kepler-65 (Chaplin et al. 2013), Kepler-25 (Albrecht et al. 2013), HD 106315 (Zhou et al. 2018; Bourrier et al. 2023), TRAPPIST-1 (Hirano et al. 2020b), TOI-1726 (Dai et al. 2020), HD 63433 (Mann et al. 2020), TOI-1136 (Dai et al. 2023), and TOI-2076 (Frazier et al. 2023).

As the spin-orbit angles of compact multiplanet systems should remain largely unaltered following the dispersal of the disk, the low stellar obliquities observed for sub-Saturns and other types of exoplanets in compact systems suggest that most planetary systems are initially formed spin-orbit aligned. Consequently, the dominant mechanism driving misalignment in single-star systems is likely not a universal process that operates indiscriminately across different types of systems but instead is inherent to those with certain postdisk dynamical histories. More broadly, support for misalignment being acquired well into in the postdisk phase rather than near the onset of system formation comes from evidence that (i) both young stellar systems ($\lesssim 100$ Myr old) and planets still embedded within their debris disks are aligned (Hirano et al. 2020a; Kraus et al. 2020; Martioli et al. 2020; Palle et al. 2020; Plavchan et al. 2020; Albrecht et al. 2022; Johnson et al. 2022) and (ii) hot Jupiter systems that are misaligned tend to be older (Hamer & Schlaufman 2022). In combination with the large spin-orbit angles commonly observed for misaligned isolated hot Jupiters and sub-Saturns, these facts are generally consistent with violent eccentric migration as the dominant

driver of misalignment (Dawson & Johnson 2018; Wu et al. 2023); identifying the most relevant migration pathway(s), however, is beyond the scope of this work.

5.3. On the Temperature–Obliquity Relation

There is an interesting discrepancy between the obliquity distributions of isolated hot Jupiters and isolated hot sub-Saturns: hot Jupiters are commonly misaligned around hot stars ($T_{\text{eff}} \gtrsim 6250$ K) but exclusively aligned around cool stars (i.e., the $T_{\text{eff}}-\lambda$ relation; see Winn et al. 2010a; Albrecht et al. 2012, 2022), while hot sub-Saturns are commonly misaligned around cool stars (and no data exist for those orbiting hot stars; see Figure 2). Realignment via tidal dissipation offers a plausible explanation for this phenomenon; cool stars are susceptible to realignment by massive hot Jupiters, while lower-mass hot sub-Saturns are less likely to realign them on timescales shorter than the system’s age (e.g., see Equation (2) of Albrecht et al. 2012). Hence, both hot Jupiters and hot sub-Saturns may indeed become misaligned through high-eccentricity migration, but only cool stars with hot Jupiters can be realigned. This tidal realignment mechanism, however, requires finely tuned parameters in order to completely realign all hot Jupiters around cool stars without leaving any on polar or retrograde orbits (Rogers et al. 2013; Li & Winn 2016), which are not seen in observations.

Alternatively or in addition to this tidal realignment scenario, it is possible that sub-Saturns are subject to misalignment mechanisms that may not operate for Jupiters. For instance, Petrovich et al. (2020) illustrate that secular resonance between an outer gas giant companion and an inner sub-Saturn, both embedded in a decaying disk, can drive the sub-Saturn to a polar orbit. The level of obliquity excitation depends on the ratio of the angular momentum between the inner and outer orbits, with nearly polar orbits preferentially excited for inner sub-Saturn-mass planets over Jupiter-mass planets. This resonance sweeping offers a natural explanation for the excess of sub-Saturns observed to be on polar orbits, regardless of stellar effective temperature (Bourrier et al. 2018; Hixenbaugh et al. 2023), as well as a potential mechanism to stunt the runaway growth of sub-Saturns since they are assumed to be embedded within an actively dispersing disk. However, this mechanism predicts similar misalignment rates for compact multiplanet and isolated systems, holding all other factors equal. This would imply that isolated sub-Saturns, which are more often misaligned, host outer companions at a higher rate than sub-Saturns in compact systems, but no statistical studies on these relative rates have yet been completed.

To explain the $T_{\text{eff}}-\lambda$ relation and spin-orbit misalignment in single-star exoplanetary systems more broadly, Hixenbaugh et al. (2023) outline a unified model wherein planets gain misalignments if other planets of comparable (or higher) mass form within their disk. Specifically, hotter, more massive stars tend to host more massive protoplanetary disks (Williams & Cieza 2011; Andrews et al. 2013; Andrews 2020), which are more likely to form multiple Jupiter-mass planets (Johnson et al. 2010; Ghezzi et al. 2018; Yang et al. 2020). These Jupiters may interact with each other to produce spin-orbit misalignments after the disk dissipates. By contrast, the limited disk mass around cooler stars is unlikely to produce more than one Jupiter-mass planet, if any (Andrews et al. 2013; Ansdell et al. 2016; Pascucci et al. 2016; Dawson & Johnson 2018;

Yang et al. 2020). As a result, these giants, which have no comparable-mass planetary perturbers, should largely retain their primordial alignments throughout the postdisk phase. Nevertheless, despite their less massive disks, cool stars may still form several sub-Saturn planets that undergo an array of dynamical interactions in the postdisk phase that are capable of exciting their stellar obliquities, analogously to multiple Jupiters around hot stars. As present-day compact systems may have avoided violent dynamical interactions, they preserve their primordial spin-orbit angle, allowing them to serve as a window into the early, undisturbed state of planetary systems.

Acknowledgments

We acknowledge the independent work on the Rossiter-McLaughlin effect measurement of TOI-5398b by Mantovan et al. We appreciate the collegiality of the team regarding the manuscript submission process.

We thank the anonymous referee for their careful review of this work and constructive feedback. We express our gratitude for the insightful discussions with George Zhou and Chelsea Huang regarding the stellar activity of young planetary systems and with Armaan Goyal regarding statistical analyses.

Data presented were obtained by the NEID spectrograph built by Penn State University and operated at the WIYN Observatory by NOIRLab, under the NN-EXPLORE partnership of the National Aeronautics and Space Administration and the National Science Foundation. These results are based on observations obtained with NEID on the WIYN 3.5 m Telescope at Kitt Peak National Observatory (PI: Songhu Wang, IU TAC). Additional NEID data were obtained through time allocated by NSF's NOIRLab (NOIRLab Prop. IDs 2022A-543544, 2023A-904842, 2023B-738235; PI: S. Yee), under the NN-EXPLORE partnership of the National Aeronautics and Space Administration and the National Science Foundation. WIYN is a joint facility of the University of Wisconsin-Madison, Indiana University, NSF's NOIRLab, the Pennsylvania State University, Purdue University, University of California, Irvine, and the University of Missouri. The authors are honored to be permitted to conduct astronomical research on Iolkam Du'ag (Kitt Peak), a mountain with particular significance to the Tohono O'odham.









M.R. acknowledges support from Heising-Simons Foundation grant #2023-4478. S.W. acknowledges support from Heising-Simons Foundation grant No. 2023-4050. We acknowledge support from the NASA Exoplanets Research Program NNH23ZDA001N-XRP (grant #80NSSC24K0153). This research was supported in part by Lilly Endowment, Inc., through its support for the Indiana University Pervasive Technology Institute. C.P. acknowledges support from ANID BASAL project FB210003, FONDECYT Regular grant 1210425, CASSACA grant CCJRF2105, and ANID+REC Convocatoria Nacional subvencion a la instalacion en la Academia convocatoria 2020 PAI77200076. The Flatiron Institute is a division of the Simons Foundation.

All the TESS data used in this paper can be found in MAST in the All Sectors, TESS Light Curves High Level Science product available at doi:10.17909/t9-nmc8-f686. This research has made use of the NASA Exoplanet Archive (NASA Exoplanet Archive 2024), which is operated by the California Institute of Technology, under contract with the National Aeronautics and Space Administration under the Exoplanet Exploration Program.

Facility: WIYN.

Software: NumPy (van der Walt et al. 2011; Harris et al. 2020), SciPy (Virtanen et al. 2020), pandas (McKinney 2010), matplotlib (Hunter 2007), allesfitter (Günther & Daylan 2021), emcee (Foreman-Mackey et al. 2013), iSpec (Blanco-Cuaresma et al. 2014), EXOFASTv2 (Eastman et al. 2019).

ORCID iDs

Brandon T. Radzom  <https://orcid.org/0000-0002-0015-382X>
 Jiayin Dong  <https://orcid.org/0000-0002-3610-6953>
 Malena Rice  <https://orcid.org/0000-0002-7670-670X>
 Xian-Yu Wang  <https://orcid.org/0000-0002-0376-6365>
 Samuel W. Yee  <https://orcid.org/0000-0001-7961-3907>
 Tyler R. Fairmington  <https://orcid.org/0000-0002-0692-7822>
 Cristobal Petrovich  <https://orcid.org/0000-0003-0412-9314>
 Songhu Wang  <https://orcid.org/0000-0002-7846-6981>

References

- Aigrain, S., Llama, J., Ceillier, T., et al. 2015, *MNRAS*, 450, 3211
 Albrecht, S., Winn, J. N., Johnson, J. A., et al. 2012, *ApJ*, 757, 18
 Albrecht, S., Winn, J. N., Marcy, G. W., et al. 2013, *ApJ*, 771, 11
 Albrecht, S. H., Dawson, R. I., & Winn, J. N. 2022, *PASP*, 134, 082001
 Andrews, S. M. 2020, *ARA&A*, 58, 483
 Andrews, S. M., Rosenfeld, K. A., Kraus, A. L., & Wilner, D. J. 2013, *ApJ*, 771, 129
 Ansdell, M., Williams, J. P., van der Marel, N., et al. 2016, *ApJ*, 828, 46
 Barnes, S. A. 2007, *ApJ*, 669, 1167
 Batygin, K. 2012, *Natur*, 491, 418
 Benz, W., Broeg, C., Fortier, A., et al. 2021, *ExA*, 51, 109
 Blanco-Cuaresma, S. 2019, *MNRAS*, 486, 2075
 Blanco-Cuaresma, S., Soubiran, C., Heiter, U., & Jofré, P. 2014, *A&A*, 569, A111
 Bourrier, V., Attia, O., Mallonn, M., et al. 2023, *A&A*, 669, A63
 Bourrier, V., Lovis, C., Beust, H., et al. 2018, *Natur*, 553, 477
 Brown, T. M., Baliber, N., Bianco, F. B., et al. 2013, *PASP*, 125, 1031
 Casasayas-Barris, N., Palte, E., Nowak, G., et al. 2017, *A&A*, 608, A135
 Chaplin, W. J., Sanchis-Ojeda, R., Campante, T. L., et al. 2013, *ApJ*, 766, 101
 Chatterjee, S., Ford, E. B., Matsumura, S., & Rasio, F. A. 2008, *ApJ*, 686, 580
 Chen, J., & Kipping, D. 2017, *ApJ*, 834, 17
 Choi, J., Dotter, A., Conroy, C., et al. 2016, *ApJ*, 823, 102
 Cosentino, R., Lovis, C., Pepe, F., et al. 2012, *Proc. SPIE*, 84461V
 Cutri, R. M., Skrutskie, M. F., van Dyk, S., et al. 2003, *yCat*, II/246
 Cutri, R. M., Wright, E. L., Conrow, T., et al. 2021, *yCat*, II/328
 Dai, F., Masuda, K., Beard, C., et al. 2023, *AJ*, 165, 33
 Dai, F., Roy, A., Fulton, B., et al. 2020, *AJ*, 160, 193
 Dawson, R. I., & Johnson, J. A. 2018, *ARA&A*, 56, 175
 Dong, J., & Foreman-Mackey, D. 2023, *AJ*, 166, 112
 Dong, J., Wang, S., Rice, M., et al. 2023, *ApJL*, 951, L29
 Dong, S., Xie, J.-W., Zhou, J.-L., Zheng, Z., & Luo, A. 2018, *PNAS*, 115, 266
 Dotter, A. 2016, *ApJS*, 222, 8
 Doyle, A. P., Davies, G. R., Smalley, B., Chaplin, W. J., & Elsworth, Y. 2014, *MNRAS*, 444, 3592
 Doyle, L., Cegla, H. M., Anderson, D. R., et al. 2023, *MNRAS*, 522, 4499
 Eastman, J. 2017, EXOFASTv2: Generalized publication-quality exoplanet modeling code, Astrophysics Source Code Library, ascl:1710.003
 Eastman, J. D., Rodriguez, J. E., Agol, E., et al. 2019, arXiv:1907.09480
 Epstein, C. R., & Pinsonneault, M. H. 2014, *ApJ*, 780, 159
 Fabrycky, D., & Tremaine, S. 2007, *ApJ*, 669, 1298
 Fabrycky, D. C., & Winn, J. N. 2009, *ApJ*, 696, 1230
 Fairmington, T. R., Nabbie, E., Huang, C. X., et al. 2024, *MNRAS*, 527, 8768
 Foreman-Mackey, D., Agol, E., Ambikasaran, S., & Angus, R. 2017, *AJ*, 154, 220
 Foreman-Mackey, D., Hogg, D. W., Lang, D., & Goodman, J. 2013, *PASP*, 125, 306
 Frazier, R. C., Stefánsson, G., Mahadevan, S., et al. 2023, *ApJL*, 944, L41
 Gaia Collaboration, Vallenari, A., Brown, A. G. A., et al. 2023, *A&A*, 674, A1
 Gelman, A., & Rubin, D. B. 1992, *StaSc*, 7, 457
 Ghezzi, L., Montet, B. T., & Johnson, J. A. 2018, *ApJ*, 860, 109

- Gray, R. O., & Corbally, C. J. 1994, *AJ*, 107, 742
- Günther, M. N., & Daylan, T. 2021, *ApJS*, 254, 13
- Gustafsson, B., Edvardsson, B., Eriksson, K., et al. 2008, *A&A*, 486, 951
- Hallatt, T., & Lee, E. J. 2022, *ApJ*, 924, 9
- Halverson, S., Terrien, R., Mahadevan, S., et al. 2016, *Proc. SPIE*, 9908, 99086P
- Hamer, J. H., & Schlaufman, K. C. 2022, *AJ*, 164, 26
- Hao, W., Kouwenhoven, M. B. N., & Spurzem, R. 2013, *MNRAS*, 433, 867
- Harris, C. R., Millman, K. J., van der Walt, S. J., et al. 2020, *Natur*, 585, 357
- Heiter, U., Lind, K., Bergemann, M., et al. 2021, *A&A*, 645, A106
- Heitzmann, A., Zhou, G., Quinn, S. N., et al. 2021, *ApJL*, 922, L1
- Hellier, C., Anderson, D. R., Triaud, A. H. M. J., et al. 2019, *MNRAS*, 488, 3067
- Hirano, T., Gaidos, E., Winn, J. N., et al. 2020b, *ApJL*, 890, L27
- Hirano, T., Krishnamurthy, V., Gaidos, E., et al. 2020a, *ApJL*, 899, L13
- Hirano, T., Suto, Y., Winn, J. N., et al. 2011, *ApJ*, 742, 69
- Hixenbaugh, K., Wang, X.-Y., Rice, M., & Wang, S. 2023, *ApJL*, 949, L35
- Hjorth, M., Albrecht, S., Hirano, T., et al. 2021, *PNAS*, 118, e2017418118
- Holcomb, R. J., Robertson, P., Hartigan, P., Oelkers, R. J., & Robinson, C. 2022, *ApJ*, 936, 138
- Holt, J. R. 1893, *AstAp*, 12, 646
- Hord, B. J., Colón, K. D., Kostov, V., et al. 2021, *AJ*, 162, 263
- Hu, Q., Rice, M., Wang, X.-Y., et al. 2024, *AJ*, 167, 175
- Huang, C., Wu, Y., & Triaud, A. H. M. J. 2016, *ApJ*, 825, 98
- Hunter, J. D. 2007, *CSE*, 9, 90
- Johnson, J. A., Aller, K. M., Howard, A. W., & Crepp, J. R. 2010, *PASP*, 122, 905
- Johnson, M. C., David, T. J., Petigura, E. A., et al. 2022, *AJ*, 163, 247
- Kanodia, S., Mahadevan, S., Ramsey, L. W., et al. 2018, *Proc. SPIE*, 10702, 107026Q
- Kipping, D. M. 2013, *MNRAS*, 435, 2152
- Knudstrup, E., & Albrecht, S. H. 2022, *A&A*, 660, A99
- Kraus, S., Le Bouquin, J.-B., Kreplin, A., et al. 2020, *ApJL*, 897, L8
- Lai, D., Foucart, F., & Lin, D. N. C. 2011, *MNRAS*, 412, 2790
- Lee, E. J. 2019, *ApJ*, 878, 36
- Li, G., & Winn, J. N. 2016, *ApJ*, 818, 5
- Louden, E. M., Winn, J. N., Petigura, E. A., et al. 2021, *AJ*, 161, 68
- Lubin, J., Wang, X.-Y., Rice, M., et al. 2023, *ApJL*, 959, L5
- Lubow, S. H., & Ogilvie, G. I. 2000, *ApJ*, 538, 326
- Mancini, L., Esposito, M., Covino, E., et al. 2018, *A&A*, 613, A41
- Mann, A. W., Johnson, M. C., Vanderburg, A., et al. 2020, *AJ*, 160, 179
- Mantovan, G., Montalto, M., Piotto, G., et al. 2022, *MNRAS*, 516, 4432
- Mantovan, G., Malavolta, L., Desidera, S., et al. 2024a, *A&A*, 682, A129
- Mantovan, G., Malavolta, L., Locci, D., et al. 2024b, *A&A*, 684, L17
- Markwardt, C. B. 2009, in *ASP Conf. Ser. 411, Astronomical Data Analysis Software and Systems XVIII*, ed. D. A. Bohlender, D. Durand, & P. Dowler (San Francisco, CA: ASP), 251
- Martioli, E., Hébrard, G., Moutou, C., et al. 2020, *A&A*, 641, L1
- Masuda, K., & Winn, J. N. 2020, *AJ*, 159, 81
- McKinney, W. 2010, in *Proc. 9th Python in Science Conf.*, ed. S. van der Walt & J. Millman (Austin, TX: SciPy), 51
- McLaughlin, D. B. 1924, *ApJ*, 60, 22
- Mounzer, D., Lovis, C., Seidel, J. V., et al. 2022, *A&A*, 668, A1
- Mustill, A. J., Davies, M. B., & Johansen, A. 2015, *ApJ*, 808, 14
- Naoz, S. 2016, *ARA&A*, 54, 441
- Naoz, S., Farr, W. M., Lithwick, Y., Rasio, F. A., & Teysandier, J. 2011, *Natur*, 473, 187
- NASA Exoplanet Archive 2024, Planetary Systems Composite Parameters, Version: 2024-03-12, NExSci-Caltech/IPAC, doi:10.26133/NEA13
- Otegi, J. F., Bouchy, F., & Helled, R. 2020, *A&A*, 634, A43
- Palle, E., Oshagh, M., Casasayas-Barris, N., et al. 2020, *A&A*, 643, A25
- Pascucci, I., Testi, L., Herczeg, G. J., et al. 2016, *ApJ*, 831, 125
- Petrovich, C. 2015, *ApJ*, 808, 120
- Petrovich, C., Muñoz, D. J., Kratter, K. M., & Malhotra, R. 2020, *ApJL*, 902, L5
- Plavchan, P., Barclay, T., Gagné, J., et al. 2020, *Natur*, 582, 497
- Pollack, J. B., Hubickyj, O., Bodenheimer, P., et al. 1996, *Icar*, 124, 62
- Queloz, D., Eggenberger, A., Mayor, M., et al. 2000, *A&A*, 359, L13
- Rasio, F. A., & Ford, E. B. 1996, *Sci*, 274, 954
- Rice, M., Gerbig, K., & Vanderburg, A. 2024, *AJ*, 167, 126
- Rice, M., Wang, S., Gerbig, K., et al. 2023a, *AJ*, 165, 65
- Rice, M., Wang, S., Howard, A. W., et al. 2021, *AJ*, 162, 182
- Rice, M., Wang, S., Wang, X.-Y., et al. 2022, *AJ*, 164, 104
- Rice, M., Wang, X.-Y., Wang, S., et al. 2023b, *AJ*, 166, 266
- Ricker, G. R., Winn, J. N., Vanderspek, R., et al. 2015, *JATIS*, 1, 014003
- Robertson, P., Anderson, T., Stefansson, G., et al. 2019, *JATIS*, 5, 015003
- Rogers, T. M., Lin, D. N. C., & Lau, H. H. B. 2012, *ApJL*, 758, L6
- Rogers, T. M., Lin, D. N. C., McElwaine, J. N., & Lau, H. H. B. 2013, *ApJ*, 772, 21
- Romanova, M. M., Ustyugova, G. V., Koldoba, A. V., & Lovelace, R. V. E. 2013, *MNRAS*, 430, 699
- Rossiter, R. A. 1924, *ApJ*, 60, 15
- Rubenzahl, R. A., Dai, F., Howard, A. W., et al. 2021, *AJ*, 161, 119
- Sanchis-Ojeda, R., Fabrycky, D. C., Winn, J. N., et al. 2012, *Natur*, 487, 449
- Sanchis-Ojeda, R., Winn, J. N., Dai, F., et al. 2015, *ApJL*, 812, L11
- Schlaflly, E. F., & Finkbeiner, D. P. 2011, *ApJ*, 737, 103
- Schwab, C., Rakich, A., Gong, Q., et al. 2016, *Proc. SPIE*, 9908, 99087H
- Siegel, J. C., Winn, J. N., & Albrecht, S. H. 2023, *ApJL*, 950, L2
- Southworth, J. 2011, *MNRAS*, 417, 2166
- Stefansson, G., Hearty, F., Robertson, P., et al. 2016, *ApJ*, 833, 175
- Stefansson, G., Mahadevan, S., Maney, M., et al. 2020, *AJ*, 160, 192
- Steffen, J. H., Ragozzine, D., Fabrycky, D. C., et al. 2012, *PNAS*, 109, 7982
- Tayar, J., Claytor, Z. R., Huber, D., & van Saders, J. 2022, *ApJ*, 927, 31
- Triaud, A. H. M. J. 2018, in *Handbook of Exoplanets*, ed. H. J. Deeg & J. A. Belmonte (Berlin: Springer), 1375
- van der Walt, S., Colbert, S. C., & Varoquaux, G. 2011, *CSE*, 13, 22
- Virtanen, P., Gommers, R., Oliphant, T. E., et al. 2020, *NatMe*, 17, 261
- Wang, S., Addison, B., Fischer, D. A., et al. 2018, *AJ*, 155, 70
- Wang, X.-Y., Rice, M., Wang, S., et al. 2022, *ApJL*, 926, L8
- Williams, J. P., & Cieza, L. A. 2011, *ARA&A*, 49, 67
- Winn, J. N., Fabrycky, D., Albrecht, S., & Johnson, J. A. 2010a, *ApJL*, 718, L145
- Winn, J. N., Johnson, J. A., Howard, A. W., et al. 2010b, *ApJL*, 723, L223
- Wright, J., Rice, M., Wang, X.-Y., Hixenbaugh, K., & Wang, S. 2023, *AJ*, 166, 217
- Wu, D.-H., Rice, M., & Wang, S. 2023, *AJ*, 165, 171
- Wu, Y., & Lithwick, Y. 2011, *ApJ*, 735, 109
- Wu, Y., & Murray, N. 2003, *ApJ*, 589, 605
- Yang, J.-Y., Xie, J.-W., & Zhou, J.-L. 2020, *AJ*, 159, 164
- Zhou, G., Rodriguez, J. E., Vanderburg, A., et al. 2018, *AJ*, 156, 93